Article

# Searching for New Ferroelectric Materials Using High-Throughput Databases: An Experimental Perspective on BiAlO₃ and BiInO₃

Megha Acharya, Stephanie Mack, Abel Fernandez, Jieun Kim, Huaiyu Wang, Kazutaka Eriguchi, Derek Meyers, Venkatraman Gopalan, Jeffrey Neaton, and Lane W. Martin*

Read Online

ACCESS | 📊 Metrics & More | 📄 Article Recommendations | S1 Supporting Information

**ABSTRACT:** Recent advances in high-throughput computational workflows are expanding the realm of materials for a range of applications. Here, we report the experimental evaluation of two such predicted candidate ferroelectric perovskite oxides: $BiAlO_3$ and $BiInO_3$. Attempts were made to synthesize polar $BiAlO_3$ and $BiInO_3$ using pulsed-laser deposition. Despite exploring a wide range of temperatures, pressures, substrates, laser fluences, and so on, attempts to grow $BiAlO_3$ with this approach resulted in no perovskite phase and decomposition to $Bi_2O_3$ and $Bi_{24}Al_2O_{40}$. Various orientations of $BiInO_3$ films were synthesized on multiple substrates, with the best crystallinity demonstrated for (200)-oriented films on MgO (001). Density-functional theory predicts two energetically competitive ground-state structures for $BiInO_3$: $Pnma$ (nonpolar) and $Pna2_1$ (polar). $BiInO_3$ films were studied by using X-ray diffraction and second-harmonic generation (SHG) and found to exhibit the nonpolar $Pnma$ structure. Temperature-dependent SHG and dielectric measurements revealed no transition to the polar structure. Optical transmission−absorption studies suggest a direct bandgap of ∼4.5 eV for $BiInO_3$. Our study underscores the need for additional descriptors for synthesizability in assessing the potential of ferroelectric candidate materials identified from high-throughput materials databases.
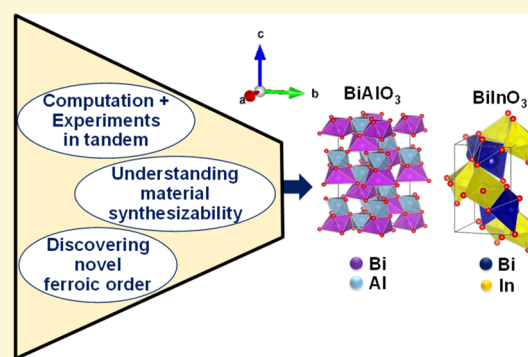
## INTRODUCTION

For much of history, the material requirements for a given application were addressable only with a (relatively) small number of known materials. Recent developments, however, have ushered in an unprecedented era in the sophisticated design of materials, thus increasing the number of possible materials at an exponential rate.[1] In pursuit of efficient approaches to accelerate the discovery, design, and realization of materials, researchers today are increasingly embracing such computationally driven design strategies and utilizing density-functional theory (DFT) calculations and experimental synthesis techniques explicitly designed to increase throughput.[2−5] Some of these predicted phases, however, are metastable and, thus, can be difficult to realize experimentally, despite being predicted to possess promising functionalities.[6−11] A relevant factor to consider in assessing whether it is possible to realize a metastable phase is the extent of metastability relative to competing structures of the same chemistry. One way to do this is through a calculation of the formation enthalpy of the phase. The formation enthalpies per atom of all the ground-state phases for a given set of elements at zero temperature and pressure, when connected, form a "hull" in energy-composition space.[12] The energy above the convex hull ($E_{hull}$) for a metastable phase with a specific composition represents the energy gained by transforming (decomposing) that phase into the ground-state

compound(s). This makes $E_{hull}$ a computed descriptor that quantifies the thermodynamic metastability of a solid.[13]

While assessing a material's (meta)stability, the modern materials designer must also explore its functional properties and potential for applications. Today, new databases are being created by using high-throughput workflows based on first-principles calculations to do just this. Multiple computational descriptors[14−16] have been introduced to screen a wide range of material classes such as binary alloys,[17−19] hydrates of metal halides,[20] and chalcopyrites.[21] Another area that has been extensively screened are the complex oxides[22−24] and, in particular, the perovskites, which can exhibit a large range of functionalities (e.g., piezoelectricity,[25] ferroelectricity,[26−28] magnetism,[29] photovoltaic effects,[30] etc.). For example, for ferroelectrics, crystal symmetry has a key role in the screening criteria since the spontaneous polarization in ferroelectrics can often be expressed as the result of ionic displacements along a polar axis relative to a nonpolar reference due to a first- or
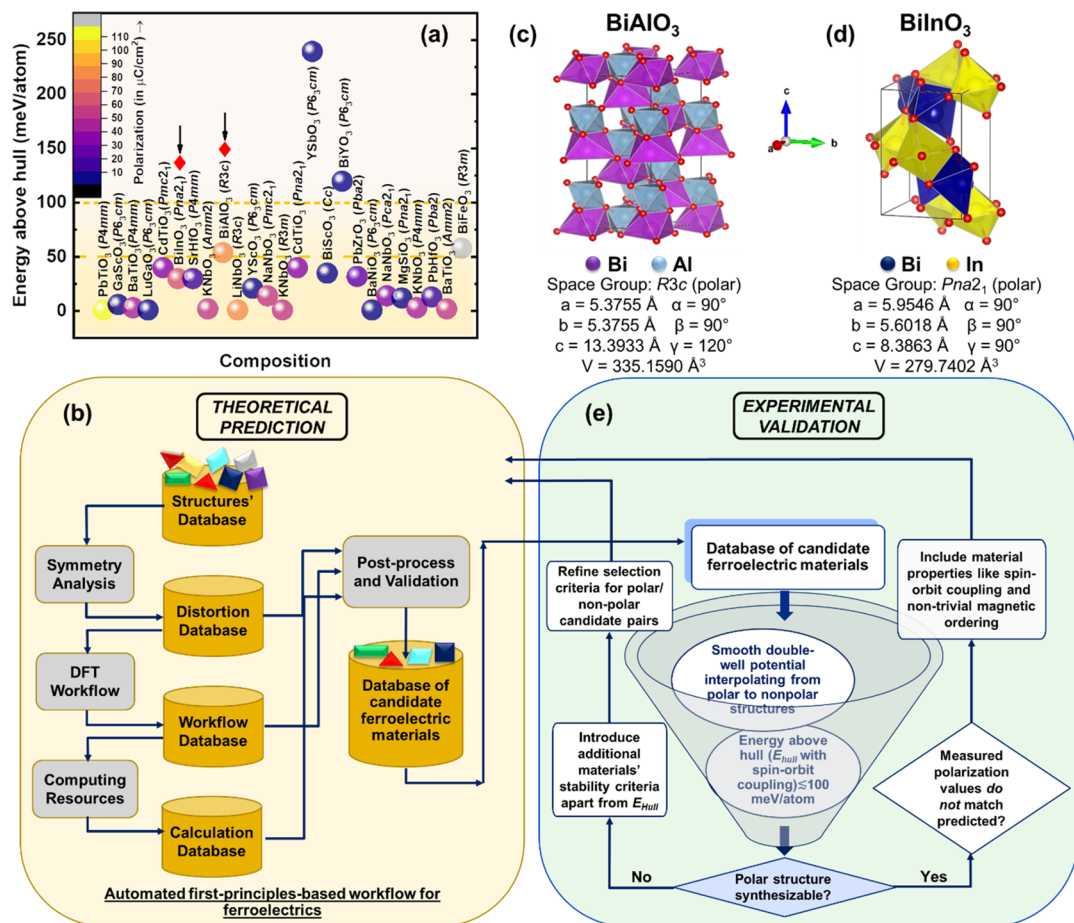
**Figure 1.** (a) A comprehensive color-map of potential $ABO_3$ oxides with their energy above convex hull/atom ($E_{hull}$) and predicted values of spontaneous polarization for their bulk crystal structures upon interpolating the atomic polarization from the transition from the nonpolar to the polar structure. (b) Automated first-principles-based workflow for ferroelectrics. Crystal structure and lattice parameters of bulk (c) $BiAlO_3$ and (d) $BiInO_3$. (e) Proposed refined workflow for searching new ferroelectric candidates.

second-order phase transition.[31] Thus, early searches for novel ferroelectric candidates combined DFT and group theory to determine nonpolar reference structures for polar structures[32−34] or used DFT calculations of phonon spectra to check for the presence of soft, or unstable, phonon modes.[35] As the field has evolved, new automated workflows that can examine all crystal classes have been developed and implemented.[26] One such workflow using DFT calculations and group theory in crystal symmetry to complete an automated and generic search through the *Materials Project* (www.materialsproject.org) database[13] has identified 255 candidate ferroelectrics with 126 of those having never been reported to be ferroelectric before.[26] Validation and augmentation of such high-throughput studies requires experimental evaluation of the new candidate ferroelectrics and, in turn, will help to accelerate the process of designing and discovering new functionalities in existing material classes.

Here, we focus on experimentally testing candidate phases put forth from such a workflow (Figures 1a,b).[26] We have chosen two relatively new and underexplored $ABO_3$ perovskite oxides, $BiAlO_3$ (Figure 1c) and $BiInO_3$ (Figure 1d), for further study. These phases were chosen because they are both isotypic to the well-studied multiferroic $BiFeO_3$[36,37] and have predicted $E_{hull}$ values that are appreciable and yet consistent with other metastable materials that have been synthesized.[38] Both feature corner-sharing $BO_6$ octahedra and a relative distortion of the

central $B$ cation away from the oxygen anions giving rise to the predicted polarization along the *c* axis. Additionally, the Wyckoff positions for the two polar phases have been summarized (Supporting Information, Table S1). Attempts were made to synthesize polar $BiAlO_3$ ($R3c$) and $BiInO_3$ ($Pna2_1$) (predicted to have spontaneous polarizations of 80.3 and 64.7 $\mu C/cm^2$, respectively[26]) by using pulsed-laser deposition. Despite testing a wide range of temperatures, pressures, substrates, laser fluences, and so on, the desired $BiAlO_3$ phase could not be synthesized with this approach; instead, films were found to decompose to the thermodynamically stable phases $Bi_2O_3$ and $Bi_{24}Al_2O_{40}$. On the other hand, (200)-, (200)-, (201)-, (002)-, and (311)-oriented $BiInO_3$ films have been successfully synthesized on $SrTiO_3$ (001), $MgO$ (001), $GdScO_3$ (110), $GdScO_3$ (001), and $MgO$ (110) substrates, respectively. Of the $BiInO_3$ phases present in the *Materials Project* database,[12] the nonpolar $Pnma$ and polar $Pna2_1$ structures are similar in energy, with the total computed energy per atom of the former being only 11 meV higher than the polar $Pna2_1$ structure. All $BiInO_3$ films were found to exhibit the $Pnma$ structure by X-ray diffraction. Attempts to produce the $Pna2_1$ structure by varying temperatures, applying electric fields, and so on were unsuccessful. Second-harmonic-generation (SHG) (down to 20 K) and dielectric (77−375 K) studies confirmed the presence of the $Pnma$ structure at all temperatures and the presence of low-loss, nearly linear dielectric response (with a room-

temperature dielectric permittivity of ~45). Despite the inability to produce the polar phase, there are limited experimental reports on $BiInO_3$ in any structure thus transmittance/reflectance measurements were used to establish a direct bandgap for $BiInO_3$ (*Pnma*) of ~4.5 eV. Beyond providing routes for synthesizing nonpolar *Pnma* $BiInO_3$, these results highlight the need for future studies to identify (additional) synthesizability criteria to aid in prioritizing theoretically predicted ferroelectric materials for experimental realization (Figure 1e).

### ■ EXPERIMENTAL SECTION

**Thin-Film Growth and Stoichiometry Determination.** Attempts to produce both $BiAlO_3$ and $BiInO_3$ were completed by using pulsed-laser deposition in an on-axis geometry with a target-to-substrate distance of 80 mm using a KrF excimer laser (248 nm, LPX 300, Coherent). For $BiAlO_3$, films were grown from a ceramic target with composition $Bi_{1.1}Al_1O_3$, wherein the 10% excess bismuth was included to account for the potential loss of bismuth during growth at high temperatures.[39−41] Depositions were attempted on multiple substrates [i.e., $LaAlO_3$ (001), $(LaAlO_3)_{0.3}(Sr_2TaAlO_6)_{0.7}$ (001), $SrTiO_3$ (001), $DyScO_3$ (110), and MgO (001)], at a range of heater temperatures (500−750 °C), across various dynamic oxygen partial pressures (1−100 mTorr), and laser fluences (0.5−1.5 J/cm²) at a laser repetition rate of 10 Hz.

For $BiInO_3$, films were grown from ceramic targets with composition $Bi_{1.1}In_1O_3$, $Bi_1In_{1.1}O_3$, and $Bi_1In_{1.2}O_3$. Various targets were tested since both bismuth and indium are highly volatile. In the end, stoichiometric films can likely be produced from different targets by varying the laser-energy density, but we focus on results from the target of composition $Bi_{1.1}In_1O_3$. Depositions were attempted on multiple substrates [i.e., $SrTiO_3$ (001), MgO (001), $GdScO_3$ (110), MgO (110), and $GdScO_3$ (001)], at a range of heater temperatures (450−650 °C), across various dynamic oxygen-partial pressures (100−200 mTorr), and laser fluences (0.7−1.5 J/cm²) at a laser repetition rate of 10 Hz. Two different growth rates (1 and 0.08 nm/s) were explored and controlled by varying the laser spot size (3.2 and 1.05 mm²) while maintaining the same overall laser fluence (~1 J/cm²). In all growths for both $BiAlO_3$ and $BiInO_3$, films were cooled from the growth pressure to room temperature at 10 °C/min in a static oxygen pressure of ~700 Torr.

Following growth, the stoichiometry of the films was analyzed via Rutherford backscattering spectrometry (RBS) using a National Electrostatics Corp. Model 5SDH pelletron tandem accelerator, where a beam of monoenergetic (3.040 MV) and collimated $\alpha$ particles (⁴He nuclei) was incident on the film surface at an incident angle $\alpha$ = 22.5°, an exit angle $\beta$ = 25.35°, and a scattering angle $\theta$ = 168°. The spectrum was fitted by using the software SIMNRA to obtain the molar ratio of the bismuth and indium for $BiInO_3$.

**Crystal Structure via X-ray Diffraction.** Diffraction studies were performed by using a high-resolution X-ray diffractometer (Panalytical, X'Pert³ MRD) with fixed-slit, 1/2° incident optics, copper K$\alpha$ radiation (1.54 Å), and a receiving slit of 0.49 mm for a PIXcel3D-Medipix3 detector. $\theta$−2$\theta$ line scans were performed to probe the structure in the direction perpendicular to the plane of the substrate, and X-ray rocking curves were completed about the $BiInO_3$ 200-, 201-, 310-, and 002-diffraction conditions for the different substrates to assess crystalline quality. Symmetric azimuthal scans were performed about the $BiInO_3$ 121-diffraction condition by varying the angle $\phi$ (azimuthal rotation) at a fixed $\chi$ (tilt) = 71.36°. X-ray pole figure measurements were conducted by simultaneous variation in $\phi$ and $\chi$ about the $BiInO_3$ 121-diffraction condition.

**Electrical and Dielectric Characterization.** When appropriate, the in-plane electrical properties for the heterostructures were investigated by using room-temperature-deposited (200 nm thick) platinum interdigitated electrodes (IDEs) patterned on the film surface with 6 $\mu$m finger spacing and 500 $\mu$m arm length. Polarization as a function of electric field (−180 to 180 kV/cm) for these IDE structures was measured by using a Precision Multiferroic Tester (Radiant

Technologies, Inc.) as a function of temperature (323−498 K). Dielectric and loss tangent measurements were done by using an E4990A impedance analyzer (Keysight Technologies) as a function of temperature (77−375 K) and frequency (1−1000 kHz) at a field of 1.67 kV/cm.

**Second-Harmonic Generation (SHG).** To analyze the potential for polar order and the point-group symmetry, SHG polarimetry analyses were performed at 20 K in an optical far-field transmission geometry at an incident angle $\theta$ = 45° as a function of the azimuthal angle ($\phi$ = 0−360°) of the incident linear polarized beam by using an 800 nm fundamental laser beam obtained from a Ti:sapphire femtosecond laser system (100 fs, 1 kHz).

**Optical Studies of Bandgap.** The optical properties (transmittance and reflectance) were measured using a PerkinElmer Lambda 950 spectrometer. To account for any contribution from the substrate, the transmittance and reflectance of the substrate were measured on a substrate without a film and used as a reference to obtain the spectrum purely from the films. The absorption was obtained from transmission and reflection measurements in the spectral range of 200−1500 nm. The absorption coefficients ($\alpha$) were calculated from the Beer−Lambert law $\left(\alpha = \frac{1}{t} \ln\left(\frac{100 - \%R}{\%T}\right)\right)$ where $t$ is the film thickness, %$R$ is the reflectance, and %$T$ is the transmittance.

**First-Principles Calculations.** DFT calculations were performed similar to those in the referenced high-throughput workflow[26] using the generalized gradient approximation of Perdew, Burke, and Ernzerhof (PBE) and the projector augmented wave formalism (PAW) as implemented in VASP.[42,43] For all calculations, Brillouin zone integrations were performed on a 4 × 3 × 4 $\Gamma$-centered $k$-grid with the tetrahedron method and a plane-wave cutoff of 520 eV. The spontaneous polarization was computed from first principles by using the Berry phase approach.[44−48] In evaluating the polarization, we used a continuous structural pathway interpolation between the nonpolar and polar structural phases of $BiInO_3$ and $BiAlO_3$, as available in the *Materials Project* database. Polarizations were computed for eight interpolated structures along the pathway between the polar and nonpolar phases; the polarization values were adjusted to the same branch, and the energy per atom was computed for each structure along the distortion pathway. The DFT computed energy difference, polarization, and amplitude of the maximum atomic displacement have all been represented and elaborated in later sections. The DFT-PBE+U bandgap, an underestimate of the true gap as is well-known, has also been computed for the polar structure. Spin−orbit coupling effects were included and treated self-consistently for all calculations due to the presence of cations with high atomic number (i.e., bismuth and indium).

### ■ RESULTS AND DISCUSSION

**$BiAlO_3$.** Similar to $BiFeO_3$, $BiAlO_3$ was predicted to have a relatively large spontaneous polarization of 80.3 $\mu$C/cm²;[26] this similarity can be rationalized as resulting from a large contribution from the stereochemical activity of the lone-pair electrons on the bismuth site, similar tolerance factors, and similar magnitudes of displacement of the $B^{3+}$ cations ($B$ = Al, Fe) and $O^{2-}$ anion from their corresponding ideal positions in the centrosymmetric structures ($R\bar{3}c$).[49] The $E_{hull}$ for $R3c$ $BiAlO_3$ is reported to be 53 meV/atom.[12] Polar $BiAlO_3$ ($R3c$) ceramics, however, have been reportedly synthesized by using high-pressure and high-temperature routes,[36,50] although there are limited studies of thin films.[51] Experimental work on bulk-ceramic versions of $BiAlO_3$ validates the metastable nature of the material since the perovskite phase was found to decompose at ~547 °C into $Al_2O_3$ and $Bi_{25}AlO_{39}$.[36,50,52,53] In addition, obtaining pure perovskite $BiAlO_3$ ceramics using solid-state reactions was shown to be difficult since, even with simultaneous application of high temperature (950 °C) and pressure (4 GPa), a majority $Bi_{25}AlO_{36−\delta}$ phase with the $\gamma$-$Bi_2O_3$ structure was
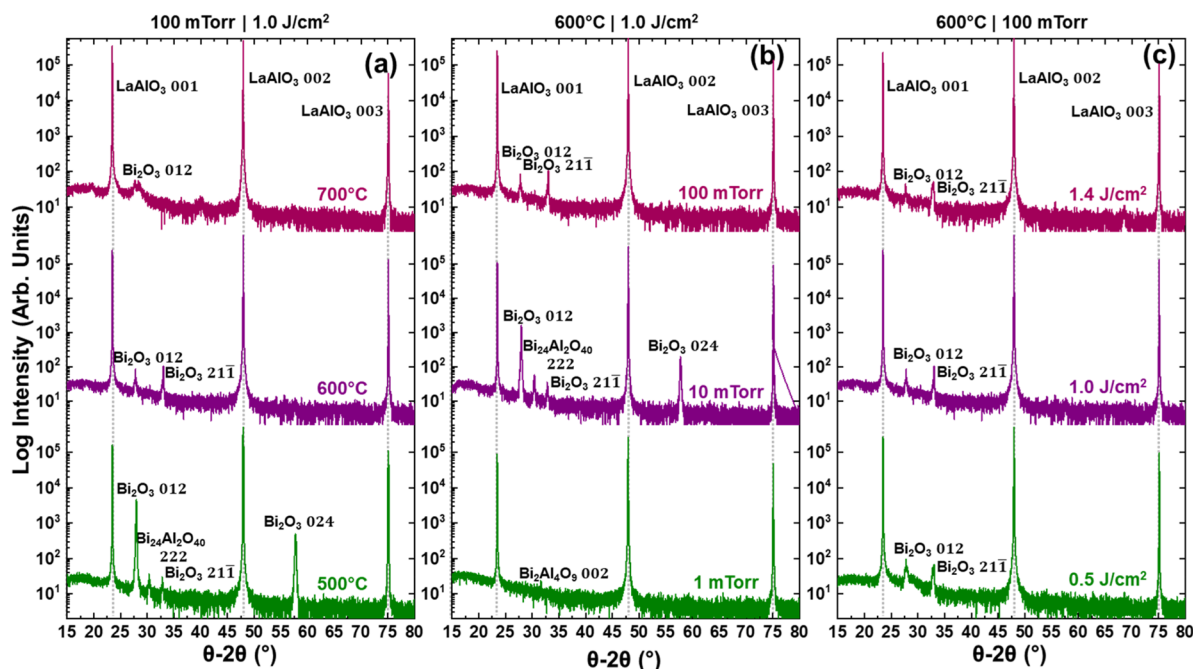
**Figure 2.** X-ray diffraction measurements for films grown from a $Bi_{1.1}AlO_3$ target as a function of (a) temperature (bottom to top: 500, 600, and 700 °C), (b) oxygen partial pressure during growth (bottom to top: 1, 10, and 100 mTorr), and (c) laser fluence (bottom to top: 0.5, 1.0, and 1.4 J/cm$^2$). The indexed phases are matched to those in ICSD PDF 00-025-1048 and ICSD PDF 00-063-0417.

reported with only ∼20% of the material possessing the desired perovskite structure.[52] Such samples exhibited linear dielectric behavior. Some have attempted to measure ferroelectric hysteresis loops for BiAlO$_3$ ceramics;[50] however, the presence of secondary phases (e.g., $Bi_2O_2CO_3$ and other unidentified impurities) together with exotic (and unexplained) temperature dependence of polarization (i.e., increasing remnant and saturation polarization with increasing temperature) necessitates further investigation. Polycrystalline thin films, reportedly synthesized on $Pt/Ti/SiO_2/Si$ (001) via sol–gel methods followed by annealing at 450–550 °C, demonstrated dielectric behavior with no evidence of ferroelectric order.[54] Another study has claimed to have synthesized and characterized polar BiAlO$_3$ (R3c) on LaAlO$_3$ (001) substrates;[51] however, this report lacks sufficient supporting information about the material structure, chemistry, and ferroelectric properties.

Building from this muddled picture, we explored a range of growth conditions to attempt to produce single-phase films. As noted in the Experimental Section, we explored growth on multiple substrates [i.e., LaAlO$_3$ (001), (LaAlO$_3$)$_{0.3}$(Sr$_2$TaAlO$_6$)$_{0.7}$ (001), SrTiO$_3$ (001), DyScO$_3$ (110), and MgO (001), with (pseudo)cubic lattice parameters ($a_{pc}$) ranging from 3.79 to 4.21 Å] at a range of heater temperatures (500–750 °C), dynamic oxygen partial pressures (1–100 mTorr), and laser fluences (0.5–1.5 J/cm$^2$). In all cases, we could not achieve a single-phase BiAlO$_3$ film. For brevity, we show the results of trials on LaAlO$_3$ (following the lead of ref 51; Figure 2) and (LaAlO$_3$)$_{0.3}$(Sr$_2$TaAlO$_6$)$_{0.7}$ (001) (Figure S1) substrates. Variations in substrate temperature (Figure 2a), growth pressure (Figure 2b), and laser fluence (Figure 2c) all resulted in multiphase films and the films were composed of Bi$_2$O$_3$ and/or Bi$_{24}$Al$_2$O$_{40}$ for all trials. Similar results were found on other substrates [i.e., SrTiO$_3$ (001), DyScO$_3$ (110), and MgO (001)], with Bi$_2$O$_3$ and Bi$_2$Al$_4$O$_9$ as the primary phases obtained (Figure S2). Despite RBS revealing nearly stoichiometric Bi:Al ratios in all cases, no aluminum-rich phases were

observed from X-ray diffraction until growth at temperatures of at least 750 °C where high-intensity diffraction peaks for the γ-Al$_2$O$_3$ phase were obtained (Figure S3). It should be noted, however, that this also corresponded to films showing lower relative bismuth content—consistent with loss of volatile bismuth at high growth temperatures. This suggests that at lower growth temperatures, while the aluminum is present in a stoichiometric ratio in the films, there is a relatively lower crystallinity to the aluminum-rich phase(s). The perovskite BiAlO$_3$ phase was not observed from X-ray diffraction studies within the range of experimental conditions explored; this confirms that the metastable BiAlO$_3$ (R3c) phase is challenging to synthesize.

These observations call into question reports of polar BiAlO$_3$ (R3c) in the literature. Furthermore, we note the thermodynamic metastability of the BiAlO$_3$ phase is not insignificant, as prior DFT studies predict $E_{hull}$ = 53 meV/atom.[12] Many high-throughput studies have reported different values for $E_{hull}$ (<50–100 meV/atom) as the limit for metastable solids suitable for synthesis, but such $E_{hull}$ limit values can be highly dependent on material chemistry and have a dearth of experimental validation.[3,16,20,25,29,30] This not only suggests the $E_{hull}$ value for BiAlO$_3$ is indeed within the range of synthesizability but also suggests that the magnitude of $E_{hull}$ is not, perhaps by itself, a sufficient criterion for synthesis, and additional criteria must exist but are yet to be identified.[38] The accuracy of the $E_{hull}$ values could be improved further by including spin–orbit coupling in the calculation of formation energy values for the bismuth-based compounds. Ultimately, our study points toward the need for developing and including additional material-synthesizability criteria (beyond $E_{hull}$) in future automated workflows and screening exercises. Besides, it suggests that robust chemical and structural data are equally essential in the experimental trials to ensure the realization of such novel materials.
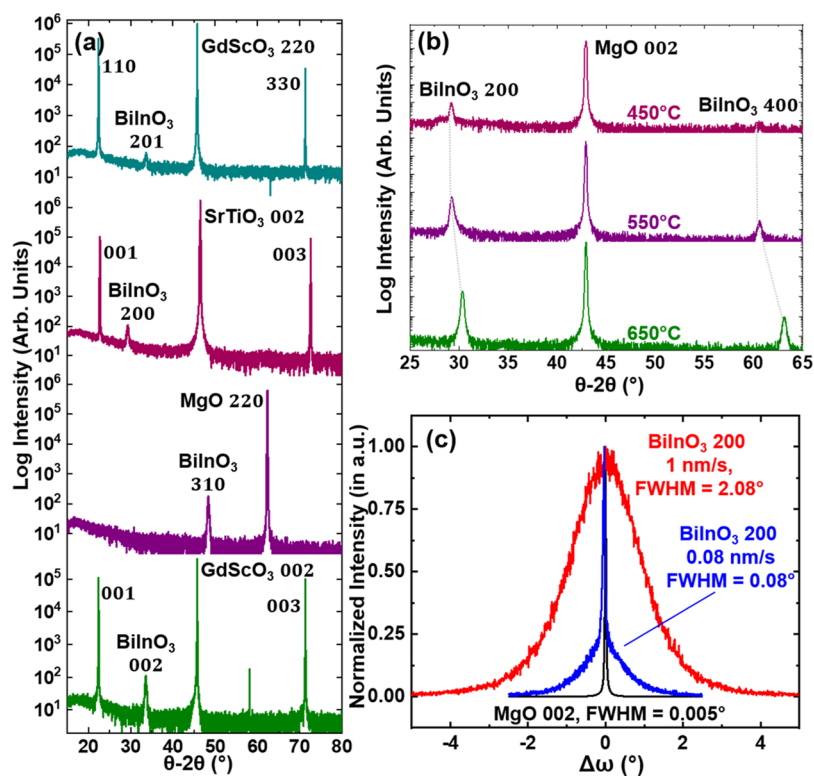
**Figure 3.** (a) X-ray diffraction scans for various orientations of $BiInO_3$ films grown on (from top to bottom) $GdScO_3$ (110), $SrTiO_3$ (001), MgO (220), and $GdScO_3$ (001) substrates. In all cases, a singly oriented $BiInO_3$ film is obtained. The indexed phases are matched to those in ICSD PDF 04-013-5373. (b) X-ray diffraction scans for (200)-oriented $BiInO_3$ films grown on MgO (001) substrates at different growth temperatures (top to bottom): 450, 550, and 650 °C. (c) Rocking curves about the $BiInO_3$ 200-diffraction condition for 1 and 0.08 nm/s growth rates as compared to that about the MgO 002-diffraction condition.

**BiInO₃.** There are a number of reasons the polar $BiInO_3$ $(Pna2_1)$ phase was selected for study. First, like $BiAlO_3$, experience in materials like $BiFeO_3$ means that the community has extensive expertise in producing bismuth-based compounds. Furthermore, apart from being a new candidate ferroelectric, other detailed first-principles calculations have predicted this phase to exhibit so-called *persistent spin texture*—the ability to maintain a uniform spin configuration in momentum space near its conduction-band minimum—which could give rise to extraordinarily long spin lifetimes for carriers.[55] In the bulk, researchers reported the synthesis of the polar $Pna2_1$ structure using a high-temperature and high-pressure approach; however, this study does not include the measurement of ferroelectric polarization or any of the properties for the synthesized material.[37] This together with the minute differences between the structures and computed energies of the nonpolar $(Pnma)$ and polar $(Pna2_1)$ phases suggests additional studies are necessary.

Building from this work, as noted in the Experimental Section, we deposited films on a range of substrates with a range of growth conditions. Overall, single-phase $BiInO_3$ films were obtained on all substrates studied [i.e., $SrTiO_3$ (001), MgO (001), $GdScO_3$ (110), MgO (110), and $GdScO_3$ (001)] in the temperature window 450−650 °C, oxygen growth pressures of 100−200 mTorr, and laser fluences 0.7−1.5 J/cm². Upon changing the substrate, different orientations of $BiInO_3$ films have been produced including (201), (200), (311), and (002) orientations on $GdScO_3$ (110), $SrTiO_3$ (001), MgO (110), and $GdScO_3$ (001), respectively (Figure 3a). The $BiInO_3$ heterostructures on these substrates, however, were found to have

generally poor crystalline quality as indicated by the corresponding X-ray rocking curves (Figure S4). For brevity, we focus here on the highest quality films produced on MgO (001) substrates. Single-phase, 80 nm thick (200)-oriented $BiInO_3$/MgO (001) heterostructures were grown at multiple temperatures (450−650 °C) (Figure 3b). The resulting (200)-oriented $BiInO_3$ films grown on MgO (001) at 550 °C were found to have the highest crystalline quality as indicated by rocking curve studies (Figure 3c) and the desired stoichiometry (Bi:In ratio is 1.08:1 from RBS; Figure S5). X-ray diffraction studies revealed that the 200- and 400-diffraction peaks for $BiInO_3$ shift to higher $\theta−2\theta$ values as the growth temperature increases as a result of changes in lattice parameters due to changing Bi:In ratios in the films as confirmed with RBS. The crystallinity of the $BiInO_3$ films can be further improved by decreasing the growth rate from 1 to 0.08 nm/s, which results in a reduction of the full width at half-maximum (FWHM) of the rocking curves about the 200-diffraction condition from 2.08° to 0.08°, respectively (Figure 3c). This is likely due to the lower growth rate providing less material per laser pulse and thus more time for the adatoms to rearrange on the substrate in the idealized locations. Armed with the ability to produce a range of $BiInO_3$ films, our attention shifted to carefully identifying the crystal symmetry of the crystalline (200)-oriented $BiInO_3$ heterostructures and to understanding if we had produced the polar or nonpolar version.

The high-throughput workflow[26] has identified two separate polar/nonpolar structure pairs for $BiInO_3$, both of which obey the symmetry criteria for a second-order phase transition. We focus on the pair with $Pna2_1$ ($E_{hull}$ = 29 meV/atom) as the polar
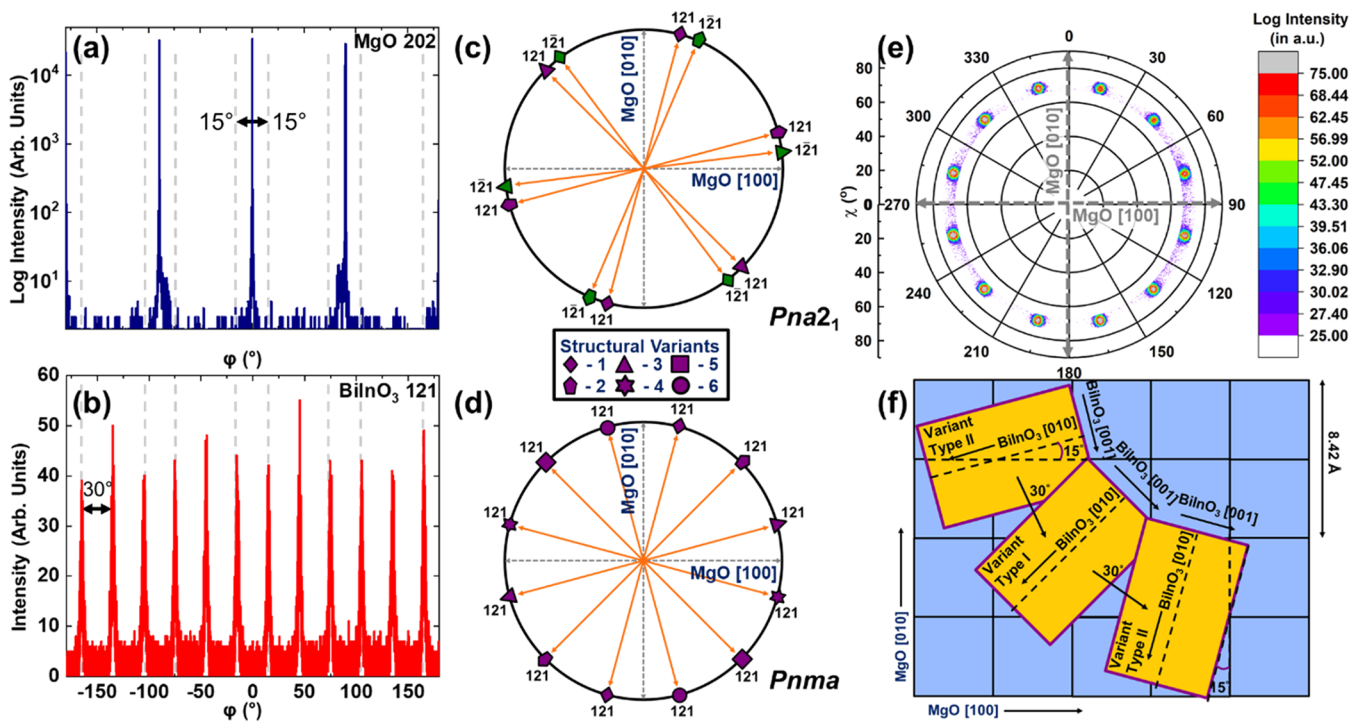
**Figure 4.** Azimuthal $\phi$ scans about the (a) MgO 202-diffraction condition and the (b) BiInO$_3$ 121-diffraction condition. Schematic representation of the expected diffraction peak positions at $\chi = 71.36°$ for the 121-diffraction conditions for (c) $Pna2_1$ symmetry with 3 structural variants and (d) $Pnma$ symmetry with 6 structural variants. (e) Experimentally measured pole figure for the (200)-oriented BiInO$_3$ film about the 121-diffraction condition ($\chi = 71.36°$). (f) Schematic showing the epitaxy of the (200)-oriented BiInO$_3$ films (yellow rectangles) grown on MgO (001) (blue squares).

structure with one of the possible nonpolar reference structures as $Pnma$ ($E_{hull}$ = 39 meV/atom).[12,26] Both the $Pnma$ (experimental lattice parameters $a = 5.95462$ Å, $b = 8.38640$ Å, and $c = 5.60185$ Å) and $Pna2_1$ (experimental lattice parameters $a = 5.95463$ Å, $b = 8.38631$ Å, and $c = 5.60182$ Å) structures have similar $E_{hull}$ values and nearly identical lattice parameters. The latter, making it nearly impossible to differentiate between the two structures using X-ray $\theta-2\theta$ line scans alone. Assessing the symmetry of the films therefore requires the use of off-axis azimuthal scans about the 121-diffraction condition. About this condition (i.e., at $\chi = 71.36°$), the polar $Pna2_1$ phase is expected to exhibit two diffraction peaks (i.e., 121 and 1$\bar{2}$1) with an angle of 128° in $\phi$ between them, while the nonpolar $Pnma$ phase has only 121 as an allowed diffraction condition. Because both the 121- and 1$\bar{2}$1-diffraction conditions have 2-fold rotational symmetry, for single-variant films the number of peaks expected in the azimuthal scans should be limited to 4 and 2 for the $Pna2_1$ and $Pnma$ structures, respectively. Upon completing such azimuthal scans about the 202-diffraction condition of the MgO substrates (Figure 4a) and the 121-diffraction condition (which corresponds to the 202-diffraction condition in pseudocubic indices) of the BiInO$_3$ films (Figure 4b), while the expected number of peaks (4) for the cubic MgO are observed to be separated by 90°, a much more complicated azimuthal scan was observed for BiInO$_3$ with 12 diffraction peaks (with the FWHM of those peaks $\approx 4°$) separated by 30° which are shifted with respect to the MgO peaks by 15° in both directions.

The observation of 12 peaks indicates that multiple structural variants must be present; 3 variants if it is the $Pna2_1$ structure (Figure 4c) or 6 variants if it is the $Pnma$ structure (Figure 4d). If the BiInO$_3$ is in the $Pna2_1$ structure, which can exhibit both 121- and 1$\bar{2}$1-diffraction conditions separated by 128° in $\phi$, there is

no way (with any number of structural variants) to explain the obtained azimuthal scan with 12 equally spaced peaks. For example, if there are 3 structural variants (Figure 4c), one would expect 12 total peaks, but those peaks should be clustered into 6 pairs (with the pairs separated by 60° and the peaks within the pair separated by just 8°) made up of the 121- and 1$\bar{2}$1-diffraction conditions from two structural variants rotated by 240° (in a clockwise sense) from one another. If BiInO$_3$, however, is in the $Pnma$ structure (Figure 4d), which exhibits only the 121-diffraction condition, one can understand the 12 observed diffraction peaks assuming there are 6 structural variants rotated by 30° with respect to each other. To further confirm this observation, pole-figure scans (Figure 4e) were obtained for the BiInO$_3$ film and likewise reveal 12 evenly spaced peaks, thus reaffirming the $Pnma$ structure with 6 in-plane rotational structural variants. Similar studies on the films grown at 1 nm/s growth rate reveal the same $Pnma$ structure and similar pole figure data (albeit with wider FWHM of the peaks; Figure S6). Armed with this information that the BiInO$_3$ is taking on the $Pnma$ structure, we can proceed to extract the lattice parameters from the diffraction studies already noted and additional reciprocal space mapping (RSM) studies (Figure S7 and Table S2) and find that $a = 6.082$ Å, $b = 8.488$ Å, and $c = 5.506$ Å. This reveals a slight volume expansion (1.63%) with respect to that reported for the bulk ceramic[37] which is likely accounted for by the slight bismuth excess in the as-grown films. Thus, we can now produce a picture of the epitaxy created in this system. The film grows entirely with the [200] of the BiInO$_3$ parallel to the out-of-plane [001] of the MgO substrate. In the plane of the film, however, things are more complicated as there are 6 rotational structural variants of the orthorhombic $Pnma$ phase (each with roughly the same fraction). There are two types of in-plane orientations. First, two structural variants are
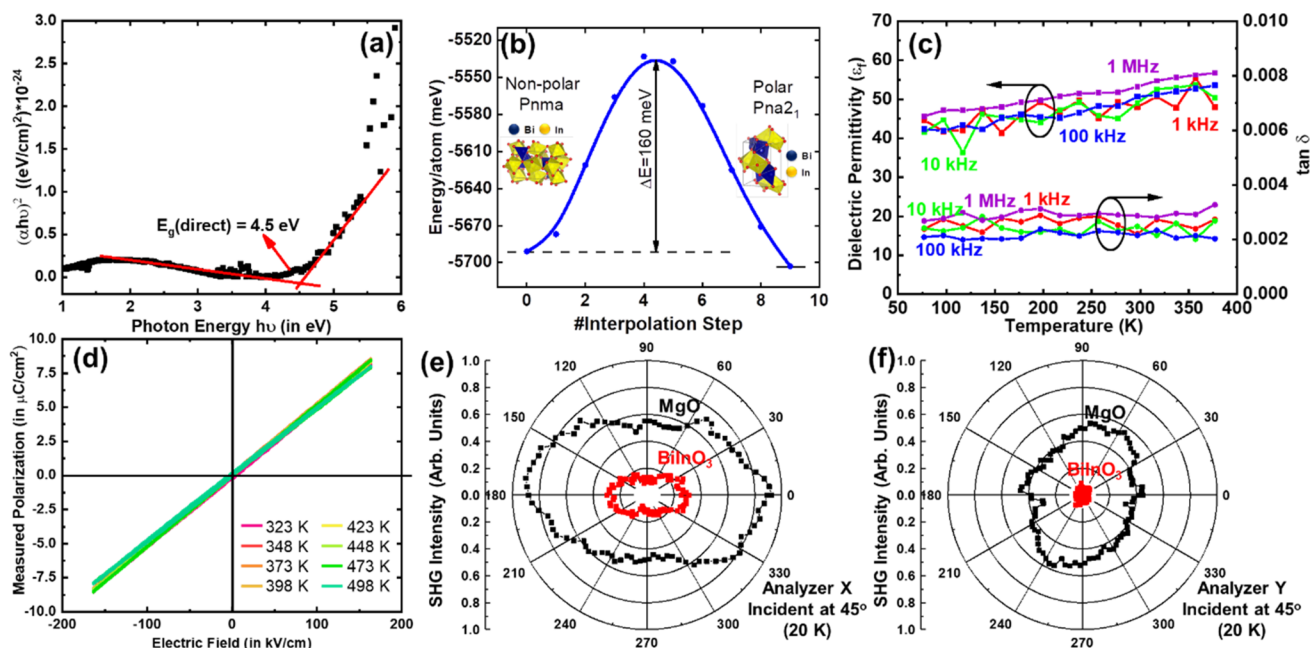
**Figure 5.** (a) Tauc plot showing the extraction of optical bandgap of the (200)-oriented $BiInO_3$ films grown on MgO (001) substrates. The inset shows the transmittance of the film and substrate as a function of photon energy. (b) DFT-based energy barrier between the nonpolar and polar $BiInO_3$ phases. The DFT approach linearly interpolates in a step-by-step manner from one structure to the other and measure the energy cost to do so. (c) Temperature-dependent dielectric permittivity (left axis) and loss tangent (right axis) measurement upon cooling from 377 to 77 K at 1, 10, 100, and 1000 kHz. (d) Polarization vs electric field upon heating from 323 to 498 K—no hysteresis is observed in this temperature range. SHG measurements for the (200)-oriented $BiInO_3$ films on MgO (001) substrates for different analyzer orientations, including analyzer (e) X and (f) Y at 20 K.

found to lie with the $BiInO_3$ [010] parallel to the MgO [110], henceforth called type I structural variants (Figure 4f). The remaining four of the rotational variants have an angle of 15° between the $BiInO_3$ [001] and the edges of the MgO substrate (i.e., [100] and [010]), henceforth called type II structural variants (Figure 4f).

Such an atypical epitaxial relationship, with multiple crystallographically equivalent variants, can be understood within the concept of dissymmetrization in bicrystallography[56] at the interface between the lattice of the film and substrate using two related yet different approaches. The first is eutaxy of the close-packed anionic planes for the film and substrate, something that is commonly observed in metal-oxide heterostructures,[57] which can explain the type I variants. The closest-packed oxygen planes for $BiInO_3$ and MgO are the {202} and {111}, respectively, and to align the intersection of these planes at the interface requires that the $BiInO_3$ grows rotated by 45° with respect to the MgO lattice (Figure S8); in essence, the $BiInO_3$ [010] is parallel to the MgO [110]. The second approach acts more locally at the interface using the planar point-group symmetry mismatch of the substrate and epilayer resulting in the type II rotational variants. Considering that the substrate [MgO (001)] and the epilayer [(200)-oriented $BiInO_3$] have planar symmetry groups $G_S$ (4mm) and $G_E$ (2mm), respectively, among the 10 possible surface-point groups (1, m, 2, 2mm, 3, 3m, 4, 4mm, 6, or 6mm[58,59]) based on the symmetry elements prevalent about the in-plane axes at the interface. The interfacial plane-group-symmetry mismatch has been found to dictate the number of rotational variants ($N_{RD}$) formed in the epilayer.[60,61] As determined by the expression in terms of group order ($n$)[62,63] for the case where the mirror-symmetry elements in the substrate and the epilayer lattice do not align with one another

$$N_{RD} = \frac{n(G_s)}{n(G_s \cap G_E)} = \frac{n(4mm)}{n(4mm \cap 2mm)} = 4$$

where ($G_s \cap G_E$) represents the intersection of the symmetry groups of the substrate−epilayer composite. Determination of the number of rotational variants, further, calls for determining their relative orientation on the substrate lattice with respect to one another. Based on anionic eutaxy, the orientation for type I variants is known (i.e., $BiInO_3$ [010] ∥ MgO [110]). Considering the rotational variants are equivalent enantiomorphs of one another, it is intuitive then that they would have identical interfacial relationship with respect to one another. The only possible way for the 4 other type II variants to be positioned on the substrate template while maintaining an equiangular (30°) orientation with respect to each other and the type I variants is by manifestating a misorientation of 15° with respect to MgO [100] and MgO [010] (Figure 4d,f). We note that attempts to obtain the $BiInO_3$ $Pna2_1$ phase were also made by growing films on $SrTiO_3$ (001) and $SrTiO_3$ (110) substrates with epitaxial 30 nm thick $SrRuO_3$ as the bottom electrode so as to provide a metallic boundary condition to perhaps favor the formation of a polar phase during cooldown from growth. In both cases, however, (200)-oriented $BiInO_3$ films with the same nonpolar $Pnma$ structure were obtained.

Having determined the structure, the dielectric and optical properties of the (200)-oriented $BiInO_3$ $Pnma$ heterostructures were measured. Transmission/reflectance studies revealed a direct bandgap of ~4.5 eV by using linear fitting of the Tauc plot (Figure 5a and Figure S9). We now turn to a discussion of the energy landscape between the polar and nonpolar structures of $BiInO_3$ (Figure 5b) which were used to compute the polarization. The energy per atom was calculated for the intermediate structures, simply constructed by linearly interpolating between the atomic positions of the polar and nonpolar

structures in eight steps,[26] revealing an energy barrier of ~160 meV/atom along the distortion pathway (Figure 5b). This is expected to be caused by the reorientation of the In−O octahedra along the distortion pathway causing the In−O bonds to reach a minimum length which is ~5% less than their equilibrium values in both the *Pnma* and *Pna*2₁ structures. Additionally, to gauge the effect of lattice strain (which can be imposed on the film through the substrate) on the height of the energy barrier, DFT calculations along the distortion pathway were completed with the theoretical lattice parameters of BiInO₃ (*Pnma* and *Pna*2₁) expanded by 2% in all directions. It was found that lattice expansion only changes the barrier height by 12 meV/atom (i.e., from 160 to 148 meV/atom). Ideally, for the transition from the nonpolar to the polar phase the energy would be a monotonically decreasing function of distortion. In this case, the energy profile suggests BiInO₃ is a possible antiferroelectric since the nonpolar and polar structures are related by symmetry, but separated by a barrier, and, therefore potentially governed by a first-order phase transition.[64] Typical computed energy barriers between polar and nonpolar phases in known antiferroelectrics, however, are somewhat smaller than observed here for BiInO₃; for instance, the barrier computed for ZrO₂ is 35 meV per formula unit[65] and <150 meV per formula unit for a range of ABC semiconductor, antiferroelectric compounds.[66] Moreover, as discussed below, double-hysteresis loops are not observed in our samples, and future studies are necessary to establish whether BiInO₃ is truly antiferroelectric, following one or more of the definitions that have been recently introduced in the literature.[64,67] In turn, temperature- and field-dependent studies were used to explore the potential for a transition to the polar *Pna*2₁ structure. Again, focusing on 80 nm (200)-oriented BiInO₃/MgO (001) heterostructures synthesized at 550 °C, the dielectric permittivity and loss tangent were measured as a function of temperature from 77 to 375 K (Figure 5c). The dielectric permittivity (~45 at room temperature) was found to vary minimally with temperature and frequency with the loss tangent being uniformly low (~0.002−0.003) across the same range. While there is some precedence for observing the *Pnma* to *Pna*2₁ phase transition in other materials below room temperature (e.g., CdTiO₃[68] at 77 K), no evidence for such a phase transition was found in BiInO₃ down to 20 K. Furthermore, in-plane studies of polarization versus electric field hysteresis loops were completed on (200)-oriented BiInO₃ heterostructures using platinum IDEs where the electric field was varied from −180 to 180 kV/cm as a function of temperature (323 to 498 K, Figure 5d); again, no sign of nonlinearity or hysteresis was observed. Apart from electrical characterization, optical measurements using SHG studies (Figure S10) were completed to examine whether the (200)-oriented BiInO₃ films can exhibit a macroscopic polar point group symmetry at low temperatures (20 K). Upon comparison of the obtained SHG response with the polar plots and the corresponding theoretical fits prevalent in the literature for polar symmetry groups like *Pna*2₁,[69,70] *Rc*,[71] *R3c*,[72] *P4mm*,[73] and so on, it is found that, consistent with the other data, the as-grown phase possesses a center of inversion symmetry, even at low temperature (Figure 5e,f). The height of the energy barrier between the *Pnma* and *Pna*2₁ structures thus appears to be too large to stabilize the polar phase. Such a value, in turn, could also serve as a useful screening parameter or computational descriptor from the DFT calculations for future automated workflows which could significantly improve the screening process for identifying new ferroelectric candidates. In addition, assessing the experimental parameters to control to preferentially synthesize the desired low-symmetry polar structure instead of a high-symmetry nonpolar structure on perovskite substrates needs further investigation both experimentally and theoretically.

## ■ CONCLUSION

The polar *R3c* phase of BiAlO₃ could not be synthesized despite extensive trials including varying substrate templates, laser-energy density, growth temperature, and oxygen-partial pressures during growth; instead, we repeatedly produced the thermodynamically stable Bi₂O₃ and Bi₂₄Al₂O₄₀ phases. It could be that the predicted $E_{hull}$ value of 53 meV/atom is an indicator that producing this phase will be challenging, although further work is required for a conclusive determination of what is most significant in obtaining the desired phase using the approaches reported here. On the other hand, the nonpolar *Pnma* phase of BiInO₃ was successfully grown on a range of substrates and with good crystallinity on MgO (001) substrates by controlling the growth rate. Temperature- and electric-field-dependent studies revealed no evidence for a transition from the nonpolar *Pnma* phase to the polar *Pna*2₁ phase, consistent with the large antiferroelectric-like energy barrier computed between these two phases (~160 meV/atom). This observation provides another possible screening parameter or metric to be considered in such workflows to identify potentially promising new polar materials. For systems with an antiferroelectric-like energy barrier between polar and nonpolar phases, careful scrutiny needs to be paid to the energy profile along the distortion pathway from the nonpolar to the polar structure where large energy barriers are prohibitive to practical structural phase transitions. One could even consider additional cutoff limits (e.g., change in *B*−O/*A*−O bond lengths) to be used for more efficient selection for polar/nonpolar structures in future workflows. Ultimately, our work highlights the importance of identifying more and better descriptors from the DFT studies— beyond $E_{hull}$ and robust cutoff values for the height of the energy barrier between polar and nonpolar phases—for these automated workflows to better focus experimental efforts and thus significantly boost the efficiency of the high-throughput screening process in identifying new candidates for ferroelectric applications.

## ■ ASSOCIATED CONTENT

### ⓈI Supporting Information

The Supporting Information is available free of charge at https://pubs.acs.org/doi/10.1021/acs.chemmater.0c01770.

> Additional structural parameters for BiAlO₃ and BiInO₃; additional X-ray diffraction studies for BiAlO₃ and BiInO₃; Rutherford backscattering spectrometry (RBS) and atomic force microscopy (AFM) studies of the BiInO₃ heterostructures; additional X-ray diffraction studies to identify the structural symmetry of the (200)-oriented BiInO₃ films grown on MgO (001) substrates; determination of lattice parameters for (200)-oriented BiInO₃ films grown on MgO (001) substrates using X-ray diffraction; nonisostructural epitaxy study of BiInO₃ (200) ‖ MgO (001) heterostructures; optical studies for bandgap measurement; second-harmonic generation (SHG) studies (PDF)

## AUTHOR INFORMATION

### Corresponding Author

**Lane W. Martin** − *Department of Materials Science and Engineering, University of California, Berkeley, Berkeley, California 94720, United States; Materials Sciences Division, Lawrence Berkeley National Laboratory, Berkeley, California 94720, United States*; Email: lwmartin@berkeley.edu

### Authors

**Megha Acharya** − *Department of Materials Science and Engineering, University of California, Berkeley, Berkeley, California 94720, United States;* orcid.org/0000-0001-9618-1771

**Stephanie Mack** − *Materials Sciences Division, Lawrence Berkeley National Laboratory, Berkeley, California 94720, United States; Department of Physics, University of California, Berkeley, Berkeley, California 94720, United States*

**Abel Fernandez** − *Department of Materials Science and Engineering, University of California, Berkeley, Berkeley, California 94720, United States*

**Jieun Kim** − *Department of Materials Science and Engineering, University of California, Berkeley, Berkeley, California 94720, United States*

**Huaiyu Wang** − *Department of Materials Science and Engineering and Materials Research Institute, Pennsylvania State University, University Park, Pennsylvania 16802, United States*

**Kazutaka Eriguchi** − *Department of Materials Science and Engineering, University of California, Berkeley, Berkeley, California 94720, United States; Materials Sciences Division, Lawrence Berkeley National Laboratory, Berkeley, California 94720, United States*

**Derek Meyers** − *Department of Materials Science and Engineering, University of California, Berkeley, Berkeley, California 94720, United States; Department of Physics, Oklahoma State University, Stillwater, Oklahoma 74078, United States*

**Venkatraman Gopalan** − *Department of Materials Science and Engineering and Materials Research Institute, Pennsylvania State University, University Park, Pennsylvania 16802, United States*

**Jeffrey Neaton** − *Materials Sciences Division and Molecular Foundry, Lawrence Berkeley National Laboratory, Berkeley, California 94720, United States; Department of Physics and Kavli Energy Nanosciences Institute, University of California, Berkeley, Berkeley, California 94720, United States*

Complete contact information is available at:
https://pubs.acs.org/10.1021/acs.chemmater.0c01770

### Notes

The authors declare no competing financial interest.

## REFERENCES

(1) Rondinelli, J. M.; et al. Accelerating functional materials discovery. *Am. Ceram. Soc. Bull.* **2013**, *92*, 14−22.

(2) Curtarolo, S.; et al. The high-throughput highway to computational materials design. *Nat. Mater.* **2013**, *12*, 191−201.

(3) Hautier, G.; et al. Phosphates as lithium-ion battery cathodes: An evaluation based on high-throughput ab initio calculations. *Chem. Mater.* **2011**, *23*, 3495−3508.

(4) Alberi, K.; et al. The 2019 materials by design roadmap. *J. Phys. D: Appl. Phys.* **2019**, *52*, 013001.

(5) Ong, S. P.; et al. Li-Fe-P-$O_2$ phase diagram from first principles calculations. *Chem. Mater.* **2008**, *20*, 1798−1807.

(6) Bernstein, J. *Polymorphism in Molecular Crystals*; Oxford University Press: 2007.

(7) Sclafani, A.; et al. Comparison of the photoelectronic and photocatalytic activities of various anatase and rutile forms of titania in pure liquid organic phases and in aqueous solutions. *J. Phys. Chem.* **1996**, *100*, 13655−13661.

(8) Li, Z.; et al. Metastable high-entropy dual-phase alloys overcome the strength−ductility trade-off. *Nature* **2016**, *534*, 227−230.

(9) Nagabhushana, G. P.; et al. Direct calorimetric verification of thermodynamic instability of lead halide hybrid perovskites. *Proc. Natl. Acad. Sci. U. S. A.* **2016**, *113*, 7717−7721.

(10) Kuech, T. F.; et al. Growth far from equilibrium: Examples from III-V semiconductors. *Appl. Phys. Rev.* **2016**, *3*, 040801.

(11) Davis, M. E.; et al. Zeolite and molecular sieve synthesis. *Chem. Mater.* **1992**, *4*, 756−768.

(12) Jain, A.; et al. Formation enthalpies by mixing GGA and GGA + U calculations. *Phys. Rev. B: Condens. Matter Mater. Phys.* **2011**, *84*, 045115.

(13) Jain, A.; et al. Commentary: The materials project: A materials genome approach to accelerating materials innovation. *APL Mater.* **2013**, *1*, 011002.

(14) Nørskov, J. K.; et al. Towards the computational design of solid catalysts. *Nat. Chem.* **2009**, *1*, 37−46.

(15) Chen, R.; et al. Topological materials discovery using electron filling constraints. *Nat. Phys.* **2018**, *14*, 55−61.

(16) Woods-Robinson, R.; et al. Assessing High-Throughput Descriptors for Prediction of Transparent Conductors. *Chem. Mater.* **2018**, *30*, 8375−8389.

(17) Curtarolo, S.; et al. AFLOWLIB.ORG: A distributed materials properties repository from high-throughput ab initio calculations. *Comput. Mater. Sci.* **2012**, *58*, 227−235.

(18) Sahni, V.; et al. Accelerated Discovery of New 8-Electron Half-Heusler Compounds as Promising Energy and Topological Quantum Materials. *J. Phys. Chem. C* **2019**, *123*, 7074−7080.

(19) Andersson, M. P.; et al. Toward computational screening in heterogeneous catalysis: Pareto-optimal methanation catalysts. *J. Catal.* **2006**, *239*, 501−506.

(20) Kiyabu, S.; et al. Computational Screening of Hydration Reactions for Thermal Energy Storage: New Materials and Design Rules. *Chem. Mater.* **2018**, *30*, 2006−2017.

(21) Yu, L.; et al. Identification of potential photovoltaic absorbers based on first-principles spectroscopic screening of materials. *Phys. Rev. Lett.* **2012**, *108*, 068701.

(22) Wang, S.; et al. Assessing the Thermoelectric Properties of Sintered Compounds via High-Throughput Ab-Initio Calculations. *Phys. Rev. X* **2011**, *1*, 021012.

(23) de Jong, M.; Chen, W.; Geerlings, H.; Asta, M.; Persson, K. A. A database to enable discovery and design of piezoelectric materials. *Sci. Data* **2015**, *2*, 150053.

(24) Ceder, G. Opportunities and challenges for first-principles materials design and applications to Li battery materials. *MRS Bull.* **2010**, *35*, 693−701.

(25) Armiento, R.; et al. Screening for high-performance piezoelectrics using high-throughput density functional theory. *Phys. Rev. B: Condens. Matter Mater. Phys.* **2011**, *84*, 014103.

(26) Smidt, T. E.; Mack, S. A.; Reyes-Lillo, S. E.; Jain, A.; Neaton, J. B. An automatically curated first- principles database of ferroelectrics. *Sci. Data* **2020**, *7*, 72.

(27) Abrahams, S. C. Structurally based predictions of ferroelectricity in seven inorganic materials with space group Pba2 and two experimental confirmations. *Acta Crystallogr., Sect. B: Struct. Sci.* **1989**, *45*, 228−232.

(28) Abrahams, S. C. Structurally based prediction of ferroelectricity in inorganic materials with point group 6mm. *Acta Crystallogr., Sect. B: Struct. Sci.* **1988**, *44*, 585−595.

(29) Singh, H. K.; et al. High-Throughput Screening of Magnetic Antiperovskites. *Chem. Mater.* **2018**, *30*, 6983−6991.

(30) Plata, J. J.; et al. Photo-sensitizing thin-film ferroelectric oxides using materials databases and high-throughput calculations. *J. Mater. Chem. A* **2019**, *7*, 27323−27333.

(31) Chandra, P.; et al. A Landau Primer for Ferroelectrics. In *Physics of Ferroelectrics*; Topics in Applied Physics; Springer: Berlin, 2007; Vol. *105*, pp 69−116.

(32) Capillas, C.; et al. A new computer tool at the Bilbao Crystallographic Server to detect and characterize pseudosymmetry. *Z. Kristallogr.* **2011**, *226*, 186−196.

(33) Igartua, J. M.; et al. Search for Pnma materials with high-temperature structural phase transitions. *Acta Crystallogr., Sect. B: Struct. Sci.* **1999**, *55*, 177−185.

(34) Kroumova, E.; et al. Prediction of new displacive ferroelectrics through systematic pseudosymmetry search. Results for materials with $Pba2$ and $Pmc2_1$ symmetry. *Acta Crystallogr., Sect. B: Struct. Sci.* **2002**, *58*, 921−933.

(35) Garrity, K. F. High-throughput first-principles search for new ferroelectrics. *Phys. Rev. B: Condens. Matter Mater. Phys.* **2018**, *97*, 024115.

(36) Belik, A. A.; et al. High-pressure synthesis, crystal structures, and properties of perovskite-like $BiAlO_3$ and pyroxene-like $BiGaO_3$. *Chem. Mater.* **2006**, *18*, 133−139.

(37) Belik, A. A.; et al. $BiInO_3$: A polar oxide with $GdFeO_3$-type perovskite structure. *Chem. Mater.* **2006**, *18*, 1964−1968.

(38) Sun, W.; et al. The thermodynamic scale of inorganic crystalline metastability. *Sci. Adv.* **2016**, *2*, e1600225.

(39) Dedon, L. R.; et al. Nonstoichiometry, Structure, and Properties of BiFeO3 Films. *Chem. Mater.* **2016**, *28*, 5952−5961.

(40) Zhu, X. H.; et al. Thickness-dependent structural and electrical properties of multiferroic Mn-doped BiFeO3 thin films grown epitaxially by pulsed laser deposition. *Appl. Phys. Lett.* **2008**, *93*, 082902.

(41) Meng, D.; et al. Enhanced spontaneous polarization in double perovskite Bi2FeCrO6 films. *J. Am. Ceram. Soc.* **2019**, *102*, 5234−5242.

(42) Perdew, J. P.; et al. Generalized Gradient Approximation Made Simple. *Phys. Rev. Lett.* **1996**, *77*, 3865−3868.

(43) Kresse, G.; et al. Efficient iterative schemes for ab initio total-energy calculations using a plane-wave basis set. *Phys. Rev. B: Condens. Matter Mater. Phys.* **1996**, *54*, 11169−11186.

(44) Resta, R.; et al. Theory of the electric polarization in crystals. *Ferroelectrics* **1992**, *136*, 51−55.

(45) Vanderbilt, D.; et al. Electric polarization as a bulk quantity and its relation to surface charge. *Phys. Rev. B: Condens. Matter Mater. Phys.* **1993**, *48*, 4442−4455.

(46) Resta, R.; et al. Macroscopic polarization in crystalline dielectrics: the geometric phase approach. *Rev. Mod. Phys.* **1994**, *66*, 899−915.

(47) King-Smith, R. D.; et al. Theory of polarization of crystalline solids. *Phys. Rev. B: Condens. Matter Mater. Phys.* **1993**, *47*, 1651−1654.

(48) Resta, R. In *Berry Phase in Electronic Wavefunctions*; Reymond, M. D., Ed.; Université, Bâtiment des sciences physiques: Lausanne-Dorigny, 1996.

(49) Sosnowska, I.; et al. Neutron diffraction studies of the crystal and magnetic structures of $BiFeO_3$ and $Bi_{0.93}La_{0.07}FeO_3$. *J. Magn. Magn. Mater.* **1996**, *160*, 384−385.

(50) Zylberberg, J.; et al. Bismuth aluminate: A new high-Tc lead-free piezo-/ferroelectric. *Chem. Mater.* **2007**, *19*, 6385−6390.

(51) Son, J. Y.; et al. Epitaxial $BiAlO_3$ thin film as a lead-free ferroelectric material. *Appl. Phys. Lett.* **2008**, *92*, 222911.

(52) Mangalam, R. V. K.; et al. Ferroelectricity in $Bi_{26-x}M_xO_{26-\delta}$ (M = Al and Ga) with the $\gamma$-Bi2O3 structure. *Solid State Commun.* **2006**, *140*, 42−44.

(53) Yu, H.; Ye, Z.-G. Dielectric, ferroelectric, and piezoelectric properties of the lead-free $(1-x)(Na_{0.5}Bi_{0.5})TiO_{3-x}BiAlO_3$ solid solution. *Appl. Phys. Lett.* **2008**, *93*, 112902.

(54) Li, Z.; et al. Novel $BiAlO_3$ dielectric thin films with high energy density. *Ceram. Int.* **2019**, *45*, 22523−22527.

(55) Tao, L. L.; Tsymbal, E. Y. Persistent spin texture enforced by symmetry. *Nat. Commun.* **2018**, *9*, 2763.

(56) Fitzgerald, G. F. Bicrystallography. *Proc. R. Soc. London A* **1997**, *386*, 95−143.

(57) Wong, F. J.; et al. Nonisostructural complex oxide heteroepitaxy. *J. Vac. Sci. Technol., A* **2014**, *32*, 040801.

(58) Terzibaschian, T.; et al. The irreducible representations of the two-dimensional space groups of crystal surfaces. Theory and applications. *Phys. Status Solidi B* **1986**, *133*, 443−461.

(59) Dresselhaus, M. S.; et al. *Group Theory, Application to the Physics of Condensed Matter*; Springer: Berlin, 2008.

(60) Grigorov, I. L.; et al. Observation and analysis of multidomain epitaxy of $\alpha$-Mn on MgO (111). *Phys. Rev. Lett.* **1999**, *82*, 5309−5312.

(61) Flynn, C. P.; et al. Structural variants in heteroepitaxial growth. *Thin Solid Films* **2001**, *389*, 116−137.

(62) Portier, R.; Gratias, D. Symmetry and Phase transformation. *J. Phys. Colloq.* **1982**, *43*, 17−34.

(63) Grundmann, M. Formation of epitaxial domains: Unified theory and survey of experimental results. *Phys. Status Solidi B* **2011**, *248*, 805−824.

(64) Rabe, K. M. Antiferroelectricity in Oxides: A Reexamination. In *Functional Metal Oxides*; Wiley-VCH Verlag GmbH & Co. KGaA: 2013; pp 221−244.

(65) Reyes-Lillo, S. E.; Garrity, K. F.; Rabe, K. M. Antiferroelectricity in thin-film $ZrO_2$ from first principles. *Phys. Rev. B: Condens. Matter Mater. Phys.* **2014**, *90*, No. 140103(R).

(66) Bennett, J. W.; et al. Orthorhombic ABC semiconductors as antiferroelectrics. *Phys. Rev. Lett.* **2013**, *110*, 017603.

(67) Tolédano, P.; et al. Theory of antiferroelectric phase transitions. *Phys. Rev. B: Condens. Matter Mater. Phys.* **2016**, *94*, 014107.

(68) Sun, P.; et al. The study on the dielectric property and structure of perovskite titanate $CdTiO_3$. *Ferroelectrics* **1998**, *217*, 137−145.

(69) Knippels, G.; et al. Mid-infrared (2.75−6.0-$\mu$m) second-harmonic generation in $LiInS_2$. *Opt. Lett.* **2001**, *26*, 617−619.

(70) Andriyevsky, B.; et al. DFT-based ab initio study of structural and electronic properties of lithium fluorooxoborate $LiB_6O_9F$ and experimentally observed second harmonic generation. *Phys. Rev. B: Condens. Matter Mater. Phys.* **2011**, *84*, 125112.

(71) Kim, T. H.; et al. Polar metals by geometric design. *Nature* **2016**, *533*, 68−72.

(72) Denev, S. A.; et al. Probing Ferroelectrics Using Optical Second Harmonic Generation. *J. Am. Ceram. Soc.* **2011**, *94*, 2699−2727.

(73) Teowee, G.; et al. Second harmonic generation from PbTiO3-based ferroelectric thin films. *J. Non-Cryst. Solids* **1992**, *147−148*, 799−802.